HEAT TRANSFER

Online ISSN:1523-1496; Publisher – Wiley.

Accepted February 27th 2021

COMPUTATION OF FERROMAGNETIC/NON-MAGNETIC NANOFLUID FLOW FROM A STRETCHING CYLINDER WITH INDUCTION AND CURVATURE EFFECTS

Md. Rezwan Bin Mizan[1]

[1] *Department of Applied Mathematics, American International University, Kuratoli, Kuril,* ***Bangladesh****.*

Email: rez179.rm@gmail.com

M. Ferdows[2]

[2] *Department of Applied Mathematics, University of Dhaka,* ***Bangladesh****.*

Email: ferdowsmohammad@yahoo.com

MD. Shamshuddin[3*]

[3] *Department of Mathematics, Vaagdevi College of Engineering (Autonomous), Bollikunta, Warangal, Telangana,* ***India.***

Email: shammaths@gmail.com, shamshuddin_md@vaagdevi.edu.in

O. Anwar Bég[4]

[4]*Professor and Director-Multi-Physical Engineering Sciences Group, Mechanical Engineering Department, School of Science, Engineering and Environment (SEE), University of Salford, Manchester,* ***UK.***

Email: gortoab@gmail.com, O.A.Beg@salford.ac.uk

S.O. Salawu[5]

[2]*Department of Physical Science, College of Pure and Applied Sciences, Landmark University, Omu-aran,* ***Nigeria****.*

Email: kunlesalawu2@gmail.com

Ali Kadir[6]

[5]*Department of Mechanical/Aeronautical Engineering, Salford University, Manchester, M54WT,* ***UK.***

Email: A.Kadir@salford.ac.uk

Corresponding author: shammaths@gmail.com, mdshamshuddin@vaagdevieng.ac.in

Contact No: +91-9866826099

Orchid Number: 0000-0002-2453-8492

ABSTRACT

Motivated by enrobing processes in manufacturing technology with intelligent coatings, this work analyses the flow of an electroconductive incompressible nanofluid with heat distribution in a boundary layer containing metallic nanoparticles or ferroparticles along an extending cylindrical body with magnetic induction effects. The quasi-linear boundary conditions for the partial derivative formulations connecting to the far stream and cylinder wall are converted to ordinary non-linear derivatives by applying appropriate similarity transformations. The emerging system of derivatives are solved by a stable, efficient spectral relaxation method (SRM). The SRM procedure is benchmarked with special limiting cases in the literature and found to corroborate exceptionally well with other studies in the literature. Here, water is taken as the base liquid containing homogenously suspended *non-magnetic* (Nimonic 80a, Silicon Dioxide (SiO_2) or *magnetic nanoparticles* Ferric Oxide (Fe_3O_4), Manganese Franklinite ($Mn\text{-}ZnFe_2O_4$),). The influence of all key parameters on the velocity and temperature distributions are displayed in graphs and tables with extensive elucidation. The wall local drag force (skin friction) and local temperature gradient (Nusselt number) are also visualized graphically for various parameters. The rate of convergence of the spectral relaxation method (SRM) convergence is compared with that of the successive over relaxation (SOR) method and observed to converge faster. Larger magnetohydrodynamic body force parameter and inverse of Prandtl magnetic number induces flow deceleration whereas it enhances temperatures. Flow acceleration is computed for SiO_2non-magnetic nanoparticles and good heat conduction augmentation is produced with nanoparticle magnetic Fe_3O_4. Rising fractional volume of the solid nanoparticle decelerates the axisymmetric flow for both non-magnetic and magnetic nanoparticles whereas it elevates the magnetic induction and temperature magnitudes.

Keywords: *Spectral relaxation method; Metallic nanoparticles; Ferro nanoparticles; Stretching cylinder; Cylinder curvature; Electromagnetic induction*

1. INTRODUCTION

The heat diffusion fluid flow in a boundary layer has many engineering usefulness, for example, enrobing system synthesis of fuel cell, extrusion of polymer sheet, coating dynamics, etc. The theory of boundary-layer in viscous Navier-Stoke equations is valuable because its can assist in maintaining a streamlined computation and physical accuracy, Schlichting [1]. This theory has therefore been implemented extensively in chemical and process mechanical engineering systems which feature viscous fluids in contact with a variety of geometries. For example, the boundary layer behavior on the stretching plates (conveyor belts) were considered by Sakiadis [2, 3]. Crane [4] extended the study done by Sakiadis on the boundary layer flow by including unvarying ambient heat in the fluid. A similarity closed form solution was found for distance and velocity linear variant. Various scientists successively adapted the Crane-Sakiadis formulation to incorporate other fluid physical properties such as radiation, porosity, exponential sheet, magnetic field, heat flux, injection/suction and so on. Illustrative studies in this area includes [5-12].

The studies enumerated above *ignored curvature* and restricted the flow medium to moving vertical or horizontal devices. Many technological mechanisms are intrinsically curved, and thus need coating boundary layer formulations that combine curvature properties. For instance, Schwarz and Wediner [13] reported that curvature surface is corresponding to overpressure propagation of flowing liquid with time-independent. Magyari et al. [14] stressed the substantial adjustments in the wall drag friction and the rate of heat distribution produced by curvature.

In the cylinder surface, radius is related to the thickness of the boundary layer and the external boundary layer flow may be considered as 2-D. For a thin cylinder the radius and the thickness of the boundary layer are taken be of equal order. For this reason, the flowing liquid in 2-D is taken as axisymmetric [15, 16]. The condition is additional complicated for contracting (or extended) cylinder surface, a process that is obtained in pipe fabrication, blow moulding, etc. [17-20]. Wang [21] established steady Newtonian analytical solutions for flows past an extending cylinder. Ishak et al. [22] performed numerical calculations for hydromagnetic convection flow du stretching cylinder and studied the velocity and heat impacts on the physical parameters. Ishak et al. [23] studied the effect of blowing/suction on the flowing liquid and heat diffusion from an extending permeable cylinder. Butt et al. [24] studied the combined effect of porous drag, magnetic field and energy irreversibility on Newtonian flow from a widening cylinder. He also observed decline in the velocity boundary film viscosity with permeability parameters and magnetic force.

In recent years, nanofluids have been increasingly deployed in industrial and technological systems. They constitute a unique subset of nanomaterials. Commonly used heat distribution liquids like ethylene glycol, water, and engine oil having small thermal conductivity when compared to metals. Therefore, dispersing solid metal particles in heat diffusion can meaningfully increase heat conduction, Nima et al. [25]. Nanofluids consists of nanoparticles distributed in the base liquids such as, water, ethylene glycol, etc. The very imperative physiognomies of nanofluids is there heat conductivity strength, Ogunseye et al. [26]. The nanoparticles adopted in the nanofluids synthesis are basically carbides (SiC), nitrides (SiN, AlN), metallic oxides (TiO_2, Al_2O_3), metallic (Cu, Al) or nanotubes carbon of diameters between the range 10 and 100nm. Sandeep et al. [27] considered transient convective of nanoliquid Nimonic 80a flowing fluid (alloy, iron, chromium, nickel)-Ethylene glycol along a vertical infinite sheet. It was detected that with a modified nanoparticle shape, rate of heat conduction is improved. Pandey and Kumar [28] reported on the flowing Cu-water nanoliquid in a stretching slippery cylinder with heat transfer boundary layer. Recently, new fluids have come up with magnetic and super magnetic particles that shows both heat and magnetic augmentation property. This kind of nanoparticle has wide-ranging usages in biomedicine, Pankhurst et al. [29], thin film smart polymer coating smart thin films [30-32], swirling bio-convection nanofluid, Shamshuddin et al. [33], nuclear smart pumping bio-inspired systems, Abdelsalam et al. [34], Quadruple solutions on nanofluid over exponential shrinking/stretching surface, Lund et al. [35], Dual solution on MHD Casson nanofluid over shrinking sheet, Lund et al. [36] and multiple solutions on nanofluid containing hybrid nanomaterials over shrinking sheet, Lund et al. [37]. Numerous students have established vigorous mathematical formulations for the flow of magnetic nano-particle through robust foundation

experimental data. Anwar Bég et al. [38] has done extensive study on hydromagnetic flow of different magnetic nanoparticles and base fluids. They observed that silver nanoparticles combined with each base fluid achieve the best temperature elevation, flow acceleration and magnetic induction. Rarani et al. [39] used sonicator-prepared iron-oxide-ethylene glycol magnetic nanofluids to show that greater electric field decreases viscosity of magnetic nanofluids and that nanofluids is observed at higher concentration of nanoparticles. Kandasamy [40] derived closed form solution for nanoliquid flow to analyze wall transpiration effects with stretching boundary flow. Shukla et al. [41] employed a homotopy method and Bejan minimization technique to simulate entropy generation in reactive magnetic nano-particle doped stagnation coating flows. Bég *et al.* [42] employed finite difference along with variational iteration methods to compute the influence of thermo-capillary convection in magnetic/ferro-nanofluid flow. Sandeep [43] studied non-Newtonian stagnation point flow of ferro-nanofluids along an elongating sheet with induced magnetic field. Qasim et al. [44] considered the hydromagnetic ferrofluid convection for an extending cylinder. Nevertheless, to the knowledge of the authors', heat transport flow of ferro-nanoliquid past a moving cylinder with diverse non-magnetic and magnetic nanoparticles and magnetic induction has thus far not been considered in the scientific reports, thus, the current study focus. In this case, a stationary applied magnetic field is considered along the longitudinally extending cylinder axis. By transformation similarity variables, the multi-physical nonlinear model is changed to ordinary system of derivatives from partial derivatives with suitable far stream and wall conditions. An alternative computational procedure known as the spectral relaxation method (SRM) is employed to have solutions to the boundary layer ordinary derivative equations which displayed a fast convergence rate. The applied simulations technique may find usefulness in the technology components coating with nano-magnetic materials.

2. CYLINDRICAL STRETCHING MODEL FLOW ANALYSIS

An axisymmetric, non-uni-directional of an incompressible moving boundary layer cylinder flow of aqueous ferro-nanoliquid is investigated. The *r*-axis is assumed along the radial direction while *x*-axis is oriented in the cylinder axis. The induced magnetic effect is significant due to huge Reynolds number and the flow is therefore distorted the magnetic field [45]. The magnetic field is normal to mutual components, $\bar{H}(H_1, H_2)$ and its aligned to the cylinder axis. The parallel component H_2 is the magnetic induced field of perpendicular element that dissipates at the cylinder surface, H_1 tends to an assumed value $H_e = xH_0$ at the periphery (free stream). The temperature at wall is T_w and temperature of far stream is T_∞ as described in **Figure 1.** Additionally, the cylinder

is taken to be elongated along the axial direction and have the linear stretching rate, $U_w = U_0 (x/l)$ in which l is the cylinder length and U_0 is constant.

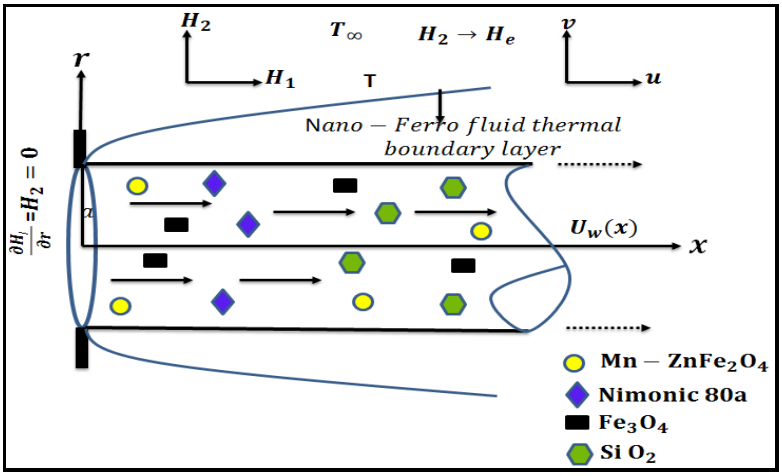

Fig. 1: Physical dimensional flow coordinate system

Extending the model [22, 44], new system of principal equations for the stretching regime, may be written as:

$$\frac{\partial (ru)}{\partial x} + \frac{\partial (rv)}{\partial r} = 0 \tag{1}$$

$$\frac{\partial (H_1 r)}{\partial x} + \frac{\partial (H_2 r)}{\partial r} = 0 \tag{2}$$

$$u\frac{\partial u}{\partial x} + v\frac{\partial u}{\partial r} - \frac{\mu_e}{4\pi\rho_f}\left(H_1\frac{\partial H_1}{\partial x} + H_2\frac{\partial H_2}{\partial r}\right) = \frac{\mu_{nf}}{\rho_{nf}}\left(\frac{\partial^2 u}{\partial r^2} + \frac{1}{r}\frac{\partial u}{\partial r}\right) \tag{3}$$

$$u\frac{\partial H_1}{\partial x} + v\frac{\partial H_1}{\partial r} - H_1\frac{\partial u}{\partial x} - H_2\frac{\partial u}{\partial x} = \eta_0\left(\frac{\partial^2 H_1}{\partial r^2} + \frac{1}{r}\frac{\partial H_1}{\partial r}\right) \tag{4}$$

$$u\frac{\partial T}{\partial x} + v\frac{\partial T}{\partial r} = \frac{k_{nf}}{(\rho c_p)_{nf}}\left(\frac{\partial^2 T}{\partial r^2} + \frac{1}{r}\frac{\partial T}{\partial r}\right) \tag{5}$$

The appropriate flow analysis boundary conditions are

$$\left.\begin{aligned} &At\ \ r = a,\quad u = U_w,\ v = 0,\ \frac{\partial H_1}{\partial r} = H_2 = 0,\ T = T_w \\ &As\ \ r \to \infty,\ u \to 0,\quad v = 0,\quad H_1 \to H_e,\ \ T \to T_\infty \end{aligned}\right\} \tag{6}$$

2.1 Nanoscale Model and Transformation

To inspire the adapted characteristic of the nanoliquid, nanofluid density is defined as ρ_{nf}, the dynamic nanofluid viscosity is described as μ_{nf}, and the heat nanofluid diffusivity is taken as α_{nf} separately as [22]:

$$\left.\begin{aligned}
\mu_{nf} &= \frac{\mu_{nf}}{(1-\phi)^{2.5}}, \\
\rho_{nf} &= (1-\phi)\rho_f + \phi\rho_s, \\
\upsilon_{nf} &= \frac{\mu_{nf}}{\rho_{nf}}, \\
(\rho c_p)_{nf} &= (1-\phi)(\rho c_p)_f + \phi(\rho c_p)_s, \\
\frac{k_{nf}}{k_f} &= \frac{(k_s+2k_f)-2\phi(k_f-k_s)}{(k_s+2k_f)+\phi(k_f-k_s)}
\end{aligned}\right\} \tag{7}$$

For uncomplicatedness, the succeeding transformation variables are used on the dimensional equations (1)-(6):

$$\left.\psi(x,r) = (\upsilon_f U_w x)^{\frac{1}{2}} a\, f(\eta),\ \eta(x,r) = \frac{r^2-a^2}{2a}\left(\frac{U_w}{\nu_f x}\right)^{\frac{1}{2}}, T_w = T_\infty + T_0(x/l), \theta(\eta) = \frac{T-T_\infty}{T_w-T_\infty}\right\} \tag{8}$$

For the momentum field, the dimensional steam function quantity is denoted as $\psi(x,r)$:

$$\left.u = \frac{1}{r}\frac{\partial\psi}{\partial r},\ v = -\frac{1}{r}\frac{\partial\psi}{\partial x}\right\} \tag{9}$$

On applying the transformation variables, the dimensionless boundary layer nanofluid derivative equations takes the form:

$$(1+2\,\gamma\,\eta)\,f''' + 2\,\gamma\,f'' + (1-\phi)^{2.5}\left\{(1-\phi)+\phi\frac{\rho_s}{\rho_f}\right\}\left[f\,f'' - f'^2 + \beta\left(g'^2 - g\,g''\right)\right] = 0 \tag{10}$$

$$\lambda(1+2\,\gamma\,\eta)g''' + 2\,\gamma\,\lambda\,g'' + \left[f\,g'' - f''g\right] = 0 \tag{11}$$

$$\frac{k_{nf}}{k_f}\left[(1+2\gamma n)\theta'' + 2\gamma\theta'\right] + \Pr\left[(1-\varphi)+\varphi\frac{(\rho c_p)_s}{(\rho c_p)_f}\right](f\theta' - f'\theta) = 0 \tag{12}$$

Proceeding with the analysis we define:

$$\phi_1 = (1-\phi)^{2.5}\left\{(1-\phi)+\phi\frac{\rho_s}{\rho_f}\right\}, \qquad \varphi_2 = \left[(1-\varphi)+\varphi\frac{(\rho c_p)_s}{(\rho c_p)_f}\right] \tag{13}$$

Eqns. (10)-(12) therefore take the absolute form:

$$(1+2\gamma\eta)\,f''' + 2\gamma\,f'' + \phi_1\left[\left(f\,f'' - f'^2\right) + \beta\left(g'^2 - g\,g''\right)\right] = 0 \tag{14}$$

$$\lambda(1+2\gamma\eta)g''' + 2\gamma\lambda g'' + [f\,g'' - f''g] = 0 \tag{15}$$

$$\frac{k_{nf}}{k_f}\left[(1+2\gamma\eta)\theta'' + 2\gamma\theta'\right] + \Pr\,\varphi_2\left(f\,\theta' - f'\theta\right) = 0 \tag{16}$$

With boundary conditions

$$\eta = 0, \quad f(0) = 0,\ f'(0) = 1,\ g''(0) = 0,\ g(0) = 0,\ \theta(0) = 1,$$
$$\eta \to \infty, \quad f'(\infty) \to 0, \quad g'(\infty) \to 1, \quad \theta(\infty) \to 0, \tag{17}$$

Here

$\gamma = \left(\frac{l\upsilon_f}{U_0 a^2}\right)^{\frac{1}{2}}$, Curvature Parameter

$\beta = \frac{\mu_e}{4\pi\rho_f}\left(\frac{H_o l}{U_o}\right)^2$, Magnetic Parameter

$\lambda = \frac{\eta_0}{\upsilon_f}$, Inverse of Prandtl magnetic Number

$\Pr = \frac{\mu_f}{\rho_f}\frac{(\rho c_p)}{k_f}$, Prandtl Number (18)

Now, the bodily measures from the point of view of engineering, wall coefficient dragging friction and wall temperature gradient (Nusselt number) can be assessed by the subsequent definitions

$$C_f = \frac{\tau_w}{\rho_f U_w^2},\ Nu_X = \frac{x q_w}{k_f (T_w - T_\infty)} \tag{19}$$

Here τ_w is the wall friction and the plate heat flux is represented by q_w which can be written as:

$$\tau_w = \mu_{nf}\left(\frac{\partial u}{\partial r}\right)_{r=a}, q_w = -k_f\left(\frac{\partial T}{\partial r}\right)_{r=a} \tag{20}$$

Hence,

$$\mathrm{Re}_x^{1/2} C_f = \frac{1}{(1-\phi)^{2.5}} f''(0), \tag{21}$$

$$\mathrm{Re}_x^{1/2} Nu_x = -\theta'(0) \tag{22}$$

3. COMPUTATIONAL SOLUTION WITH SPECTRAL RELAXATION METHOD (SRM)

Using spectral collocation, a system of large nonlinear equations is reduced to smaller systems of linear equations by simple iteration technique which is known as the spectral relaxation method. Motsa [46] has described this method in detail. The method has been applied in numerous viscous fluid dynamics problems including micropolar geophysical plume dynamics, Anwar et al. [47], exothermically reacting gel propulsion, Anwar et al. [48], von Kármán swirling viscoelastic flow, Motsa and Makukula [49], unsteady rotating flows with activation energy and species binary reaction, Awad et al. [50] and transient mixed convection in magnetic nanofluids from stretching or shrinking surfaces. SRM is correspondingly used on the quasi-linear coupled systems of derivative equations. The transformed Eqs. (14)-(17) is discretized by following the SRM algorithm procedures which involves 3 stages:

1. Set $f'(\eta) = F(\eta)$ for the equation order to be reduced.

2. $f(\eta)$ is evaluated from previous computation (symbolized by $f_r(\eta)$), and linear terms in $F(\eta)$ are calculated at present stage (represented by $F_{r+1}(\eta)$) and all other terms are previously known from the existing stage.
3. The same computation schemes is followed for other dependent variables.

This method is equivalent to the Gauss-Seidel technique. The algorithm stated above leads to. Chebyshev spectral collocation methods ([51], [52]). Spectral methods have remarkably high accuracy and are easy to implement within simple domains.

Eqns. (14)- (17) now become:

$$(1+2\gamma\eta)F''_{r+1}+2\gamma F'_{r+1}+\phi_1\left\{f_r\ F'_{r+1}-F_r^2+\beta(G_r^2-g_rG'_{r+1})\right\}=0 \tag{23}$$

$$f'_{r+1}=F_{r+1},\qquad f_{r+1}(0)=0 \tag{24}$$

$$\lambda(1+2\gamma\eta)G''_{r+1}+2\gamma\lambda G'_{r+1}+\left\{f_{r+1}\,G'_{r+1}-F'_{r+1}g_r\right\}=0 \tag{25}$$

$$g'_{r+1}=G_{r+1},\qquad g_{r+1}(0)=0 \tag{26}$$

$$\frac{k_{nf}}{k_f}\left[(1+2\gamma\eta)\theta''_{r+1}+2\gamma\theta'_{r+1}\right]+\mathrm{Pr}\ \phi_2\left(f_{r+1}\theta'_{r+1}-F_{r+1}\theta_{r+1}\right)=0 \tag{27}$$

The associated boundary conditions:

$$F_{r+1}(0)=1\qquad F_{r+1}(\infty)=0 \tag{28}$$

$$\theta_{r+1}(0)=1\qquad \theta_{r+1}(\infty)=0 \tag{29}$$

$$g_{r+1}(0)=1\qquad G_{r+1}(\infty)=1 \tag{30}$$

To solve (23)-(30) we used Chebyshev spectral collocation technique ([50], [51]). The spectral technique is applied in the domain [-1,1]. The transformation $\eta=L\frac{(\tau+1)}{2}$ is used to map $[0,L]$ to [-1,1], where L is large enough to deal with infinity.

The product of the matrix vector is defined as

$$\frac{df_r}{d\eta}=\sum_{k=0}^{N}D_{lk}\,f_r(\tau_k)=Df_r,\qquad l=0,1,2,3,.....,N \tag{31}$$

Where N+1 is the number of grid points, $D=\frac{2A}{L}$ and f is defined as:

$$f=[f(\tau_0),f(\tau_1),f(\tau_2),f(\tau_3),.....,f(\tau_N)]^T \tag{32}$$

As a power of D, higher derivative orders are gotten:

$$f_r^{(p)}=D^p f_r \tag{33}$$

Where the derivative order is p . Utilizing the spectral method to Eqns. (23) to (27) to have:

$$A_1F_{r+1}=B_1,\quad F_{r+1}(\tau_N)=1,\quad F_{r+1}(\tau_0)=0 \tag{34}$$

$$A_2f_{r+1}=B_2,\quad f_{r+1}(\tau_N)=0, \tag{35}$$

$$A_3G_{r+1}=B_3,\quad G_{r+1}(\tau_0)=1, \tag{36}$$

$$A_4 g_{r+1} = B_4, \quad g_{r+1}(\tau_N) = 0, \tag{37}$$

$$A_5 \theta_{r+1} = B_5, \quad \theta_{r+1}(\tau_N) = 1, \quad \theta_{r+1}(\tau_0) = 0 \tag{38}$$

Where,

$$A_1 = diag\,(1+2\gamma\eta)D^2 + diag\,(2\gamma + \phi_1\ f_r)D \tag{39}$$

$$B_1 = \phi_1 \left\{F_r^2 - \beta(G_r^2 - g_r G'_{r+1})\right\} \tag{40}$$

$$A_2 = D, \ B_2 = F_{r+1} \tag{41}$$

$$A_3 = diag\ \left(\lambda\left(1+2\gamma\eta\right)\right)D^2 + diag\left(2\gamma\lambda + f_{r+1}\right)D - F'_{r+1}\,I, \qquad B_3 = 0, \tag{42}$$

$$A_4 = D, \ B_4 = G_{r+1} \tag{43}$$

$$A_5 = diag\,[\frac{k_{nf}}{k_f}\left(1+2\gamma\eta\ \right)]D^2 + diag\ (2\gamma + \Pr\ \phi_2 f_{r+1})\,D - \Pr\ \phi_2\, F_{r+1}, \qquad B_5 = 0 \tag{44}$$

In Eqn. (42), the identity matrix is *I*. Diag [ ] refers to a diagonal matrix, f, F, g, G, θ correspondingly, when calculated at the grid points and the iteration number is signified by the subscript *r*. The initial assumptions for the functions is chosen to be compatible with boundary conditions. Therefore, we make the following guess for the initial value of the functions:

$$f_0 = 1 - e^{-\eta}, \qquad F_0(\eta) = e^{-\eta}, \quad g(\eta) = e^{-\eta}, \qquad G(\eta) = 1, \qquad \theta(\eta) = e^{-\eta} \tag{45}$$

For collocation point, *N*=80 is considered to have a precise results. Taking from the preliminary guesstimate (45), the SRM technique is used to achieve the resulting condition

$$\max\,(F_{r+1} - F_{r\infty}, G_{r+1} - G_{r\infty}, \quad \theta_{r+1} - \theta_{r\infty}) \le \varepsilon_r \tag{46}$$

Where, ε_r is a error tolerance taken to be 10^{-6} . We have used the spectral method to fast the convergence of iterative by introducing relaxation parameter ω on Eqns. (34)-(38):

$$A_1 F_{r+1} = (1-\omega)\,A_1 F_r + \omega B_1 \tag{47}$$

$$A_2 G_{r+1} = (1-\omega)\,A_2 G_r + \omega B_2 \tag{48}$$

$$A_3\,\theta_{r+1} = (1-\omega\,)\,A_3\ \ \theta_r + \omega\ \ B_3 \tag{49}$$

Subject to the same conditions, the value of ω depends upon the input terms that provides the good convergence depending on the input parameters magnitude. We have taken ω in the range 0.74< ω <1 which correspond to under relation (SOR, ω <1). An assessment table of results for the SRM with SOR and the basic SRM are presented in **Table 1** for the wall temperature gradient (various nanoparticles is examined). It is seen that SRM with SOR quickens the rate of convergence.

Table 1: Assessment of wall temperature gradient convergence (Nusselt number) for SRM with SOR and SRM

Terns	Nanoparticles	Nusselt number	Iterations required	
			Basic SRM	SRM with SOR
$\gamma = 0.5, \beta = 0.14, \lambda = 0.5,$ $\phi = 0.1, 0.15, \Pr = 0.72$	Mn-$ZnFe_2O_4$	0.14	37	19
$\gamma = 0.5, \beta = 0.1, \lambda = 0.5,$ $\phi = 0.1, 0.15, \Pr = 0.72$	SiO_2	1.2356	38	21
$\gamma = 1.1, \beta = 0.1, \lambda = 0.5,$ $\phi = 0.1, 0.15, \Pr = 0.72$	Nimonic 80a	1.1249	33	15
$\gamma = 0.5, \beta = 0.1, \lambda = 0.5,$ $\phi = 0.1, 0.15, \Pr = 0.72$	Fe_3O_4	1.2233	35	20

4. VALIDATION OF SRM RESULTS AND DISCUSSION

A broad computed series of SRM has been carried out in **Figs. 2a-11b**. A thermo-dynamical properties of parameters sensitivity with water based fluid for four nanoparticles are examined, two are non-magnetics (SiO_2 and Nimonic 80a), and two are magnetics (Mn-$ZnFe_2O_4$, and Fe_3O_4) are given in the **Table 2** ([44, 53]).

The exactness of MATLAB symbolic software for spectral relaxation method (SRM) in standard form is confirmed with models from available articles. Using $\phi_1 = \phi_2 = 1 = k_{nf} / k_f$, $\phi = \gamma = \lambda = \beta = 0$ and changing the value of $\Pr$, the adopted method (SRM) results are compared for the wall temperature gradient (Nusselt number) with the asymptotic solutions of Wang [54] and finite difference of Keller-box solution procedure by Khan and Pop [55]. The obtained computed results are established showing a good quantitative agreement with others as revealed in **Table 3,** the accuracy of the solution technique (SRM) is then defensibly. $\Pr < 1$ denotes small fluid heat conductivity, $\Pr = 7$ represents water while polymers takes $\Pr > 20$.

Table 2: Thermo physical property of nanoparticles and base fluid.

	ρ (kg/m^3)	c_p (J/Kg-K)	k (W/m-K)
Water	997.1	4179	0.613
Fe_3O_4	5180	670	9.7
Mn-$ZnFe_2O_4$	4900	800	5
Nimonic 80a	8190	448	112
SiO_2	2220	745	1.38

Table 3: Assessment of Prandtl number on the asymptotic Nusselt number solutions

Pr	Present Study	Wang [54]	Khan and Pop [55]
0.2	0.1691012	0.1697	0.1691
0.7	0.4539616	0.4539	0.4539
2	0.9113768	0.9114	0.9114
7	1.8954305	1.8954	1.8954
20	3.3539414	3.3539	3.3539
70	6.4621077	6.4622	6.4622

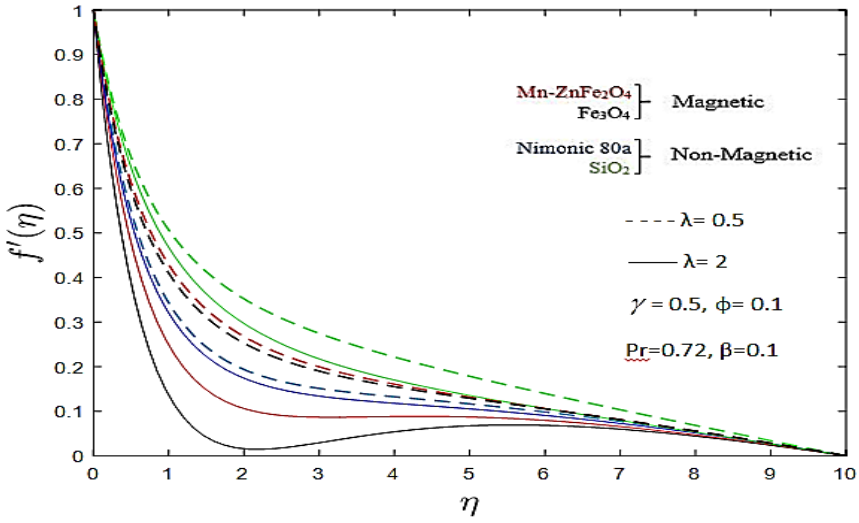

Figure 2a: Flow rate fields, $f'(\eta)$ for various λ and various nano-ferrofluids, with $\gamma = 0.5, \beta = 0.1, \lambda = 0.5, \phi = 0.1, \Pr = 0.72$

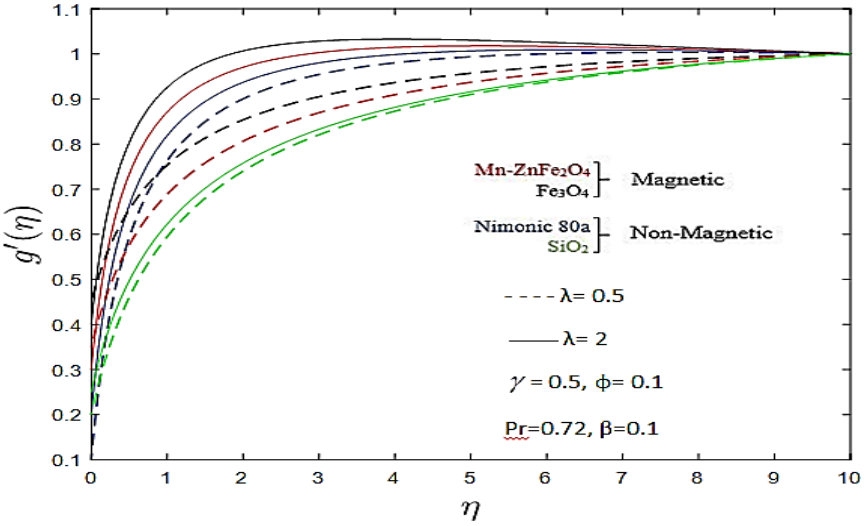

Figure 2b: Stream magnetic gradient function, $g'(\eta)$ for various λ and various nano-ferrofluids, with $\gamma = 0.5, \beta = 0.1, \lambda = 0.5, 2, \phi = 0.1, \Pr = 0.72$

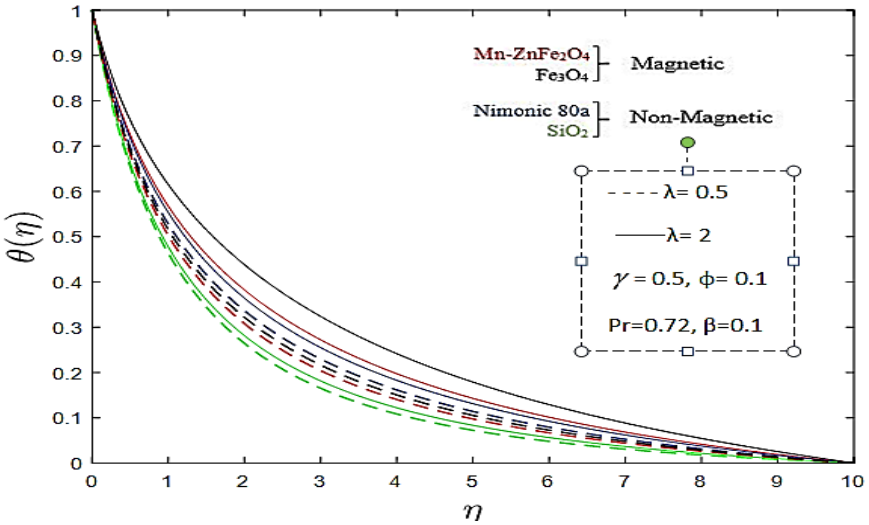

Figure 2c: Temperature fields, $\theta(\eta)$ for various λ and various nano-ferrofluids, with $\gamma = 0.5, \beta = 0.1, \lambda = 0.5, 2, \phi = 0.1, \Pr = 0.72$

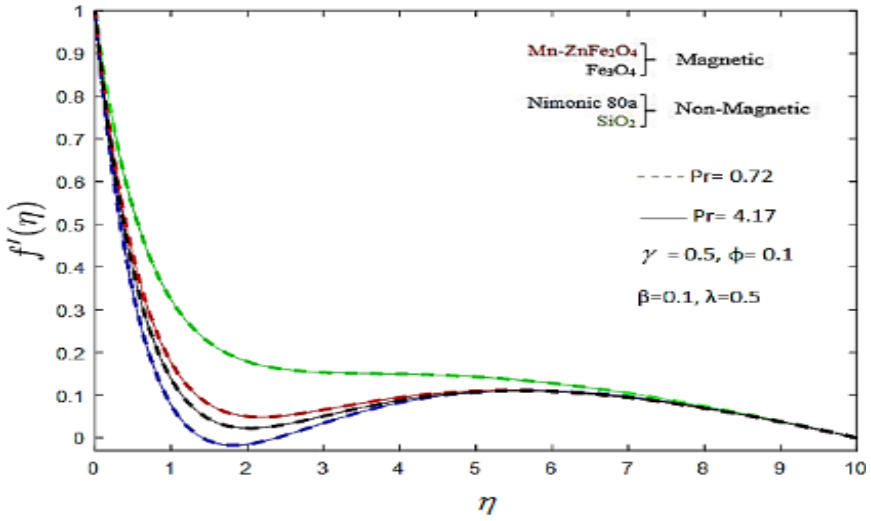

Figure 3a: Velocity profiles, $f'(\eta)$ for various Pr and different nano-ferrofluids, with $\gamma = 0.5, \beta = 0.1, \lambda = 0.5, \phi = 0.1, \mathrm{Pr} = 0.72, 4.17$

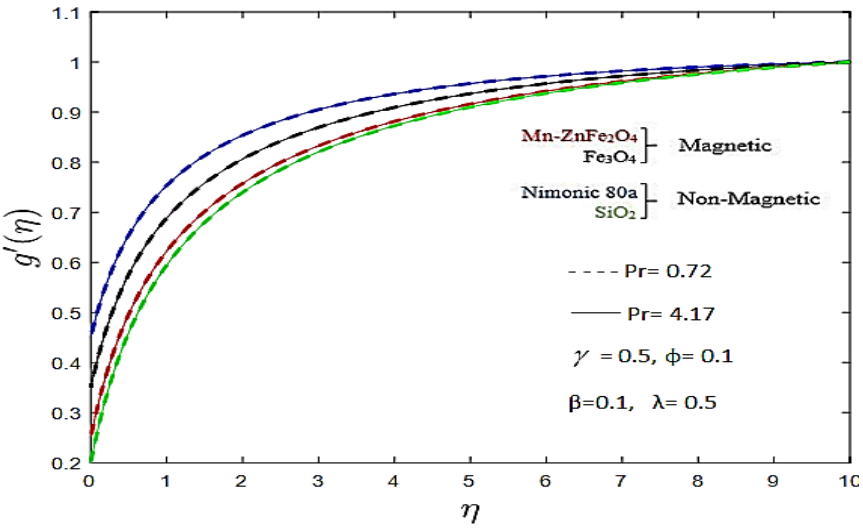

Figure 3b: Stream magnetic gradient function, $g'(\eta)$ for various Pr and various nano-ferrofluids, with $\gamma = 0.5, \beta = 0.1, \lambda = 0.5, \phi = 0.1, \mathrm{Pr} = 0.72, 4.17$

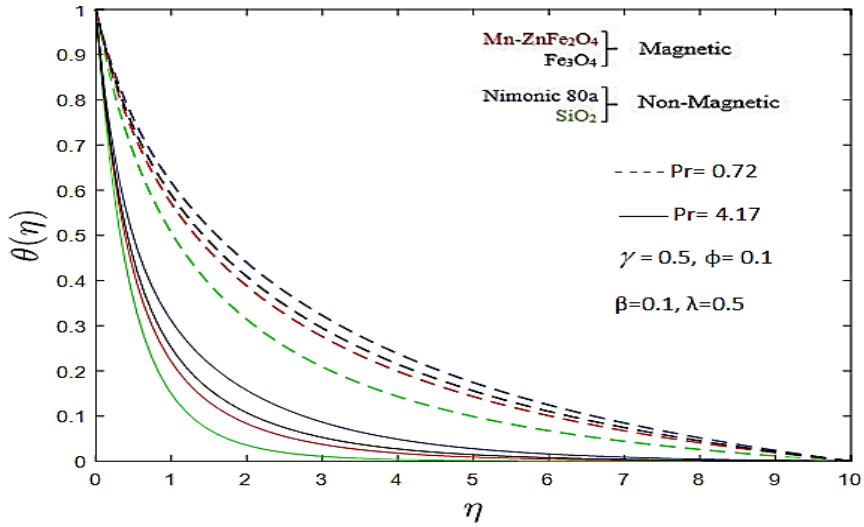

Figure 3c: Temperature profiles, $\theta(\eta)$ for various Pr and different nano-ferrofluids, with $\gamma = 0.5, \beta = 0.1, \lambda = 0.5, \phi = 0.1, \mathrm{Pr} = 0.72, 4.17$

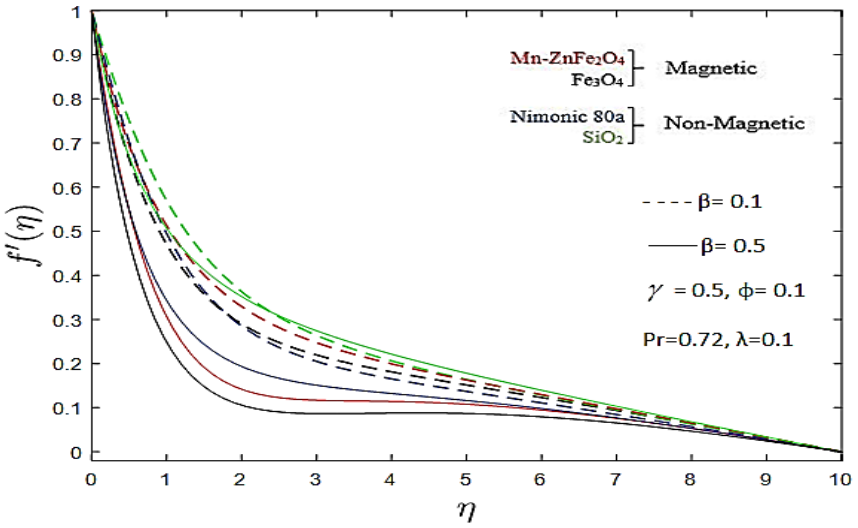

Figure 4a: Flow velocity field, $f'(\eta)$ for various β and various nano-ferrofluids, with $\gamma = 0.5$, $\beta = 0.1, 0.5$, $\lambda = 0.5$, $\phi = 0.1$, $\mathrm{Pr} = 0.72$

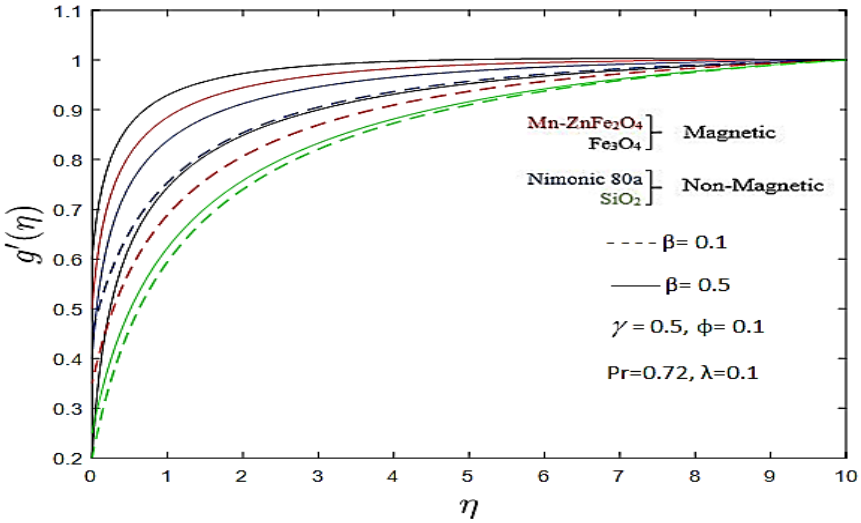

Figure 4b: Stream magnetic gradient function, $g'(\eta)$ for various β and various nano-ferrofluids, with $\gamma = 0.5$, $\beta = 0.1, 0.5$, $\lambda = 0.5$, $\phi = 0.1$, $\mathrm{Pr} = 0.72$

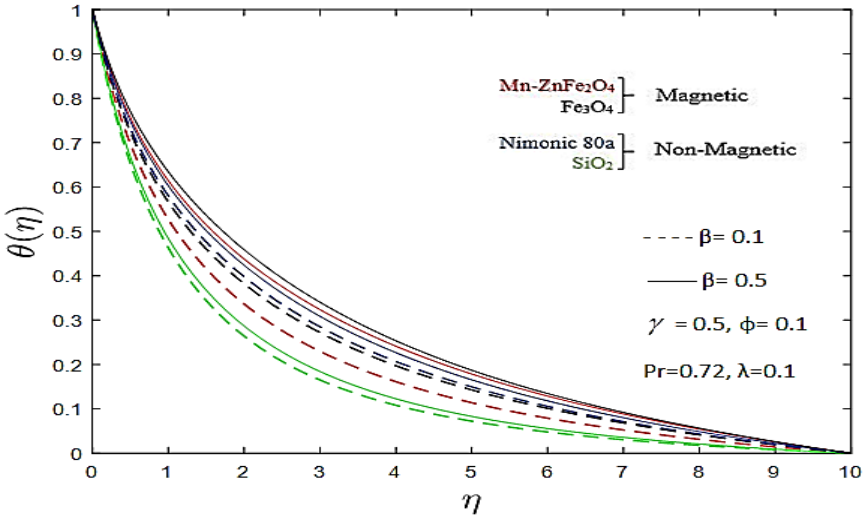

Figure 4c: Temperature fields, $\theta(\eta)$ for various β and various nano-ferrofluids, with $\gamma = 0.5$, $\beta = 0.1, 0.5$, $\lambda = 0.5$, $\phi = 0.1$, $\mathrm{Pr} = 0.72$

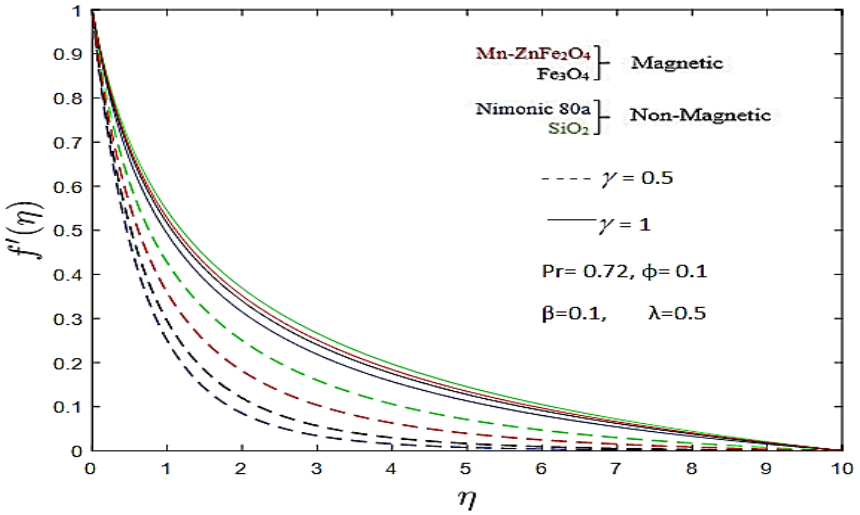

Figure 5a: Velocity field, $f'(\eta)$ for various γ and various nano-ferrofluids, with $\gamma = 0.5, 1$, $\beta = 0.1$, $\lambda = 0.5$, $\phi = 0.1$, $\mathrm{Pr} = 0.72$

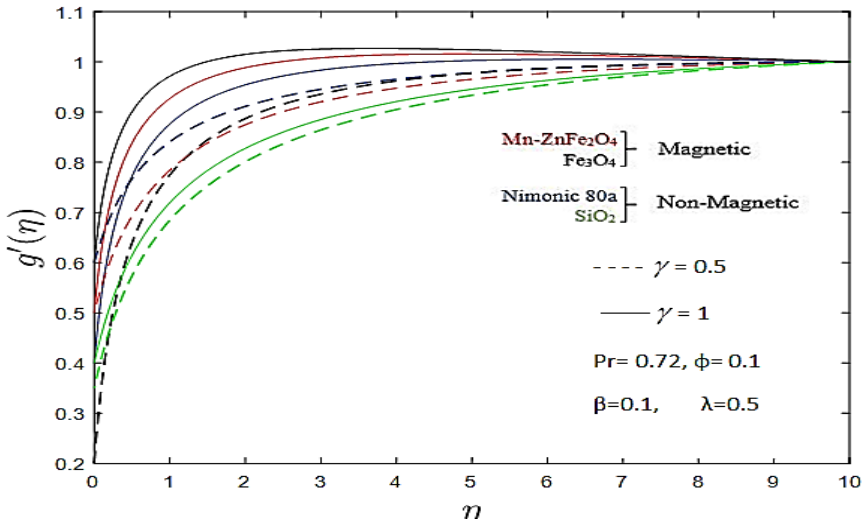

Figure 5b: Stream magnetic gradient function, $g'(\eta)$ for various γ and various nano-ferrofluids, with $\gamma = 0.5, 1$, $\beta = 0.1$, $\lambda = 0.5$, $\phi = 0.1$, $\mathrm{Pr} = 0.72$

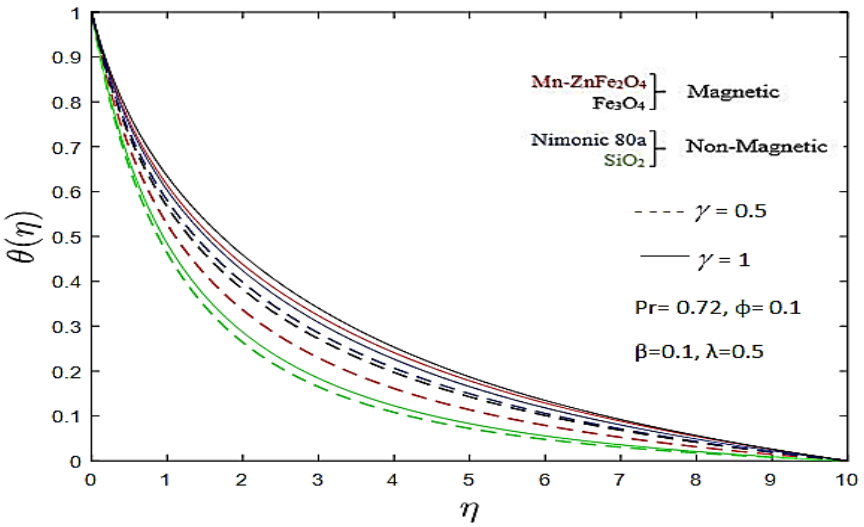

Figure 5c: Temperature fields, $\theta(\eta)$ for various γ and various nano-ferrofluids, with $\gamma = 0.5, 1$, $\beta = 0.1$, $\lambda = 0.5$, $\phi = 0.1$, $\mathrm{Pr} = 0.72$

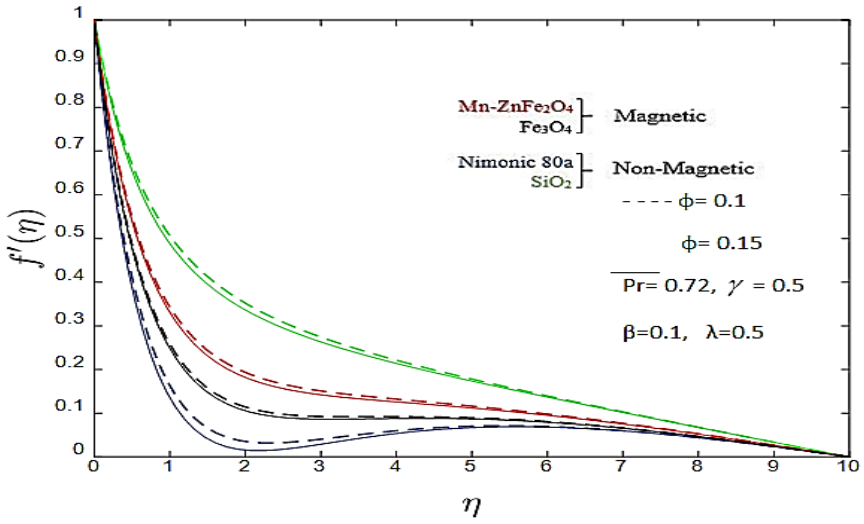

Figure 6a: Flow velocity fields, $f'(\eta)$ for various ϕ and various nano-ferrofluids, with $\gamma = 0.5, 1, \beta = 0.1, \lambda = 0.5, \phi = 0.1, 0.15, \Pr = 0.72$

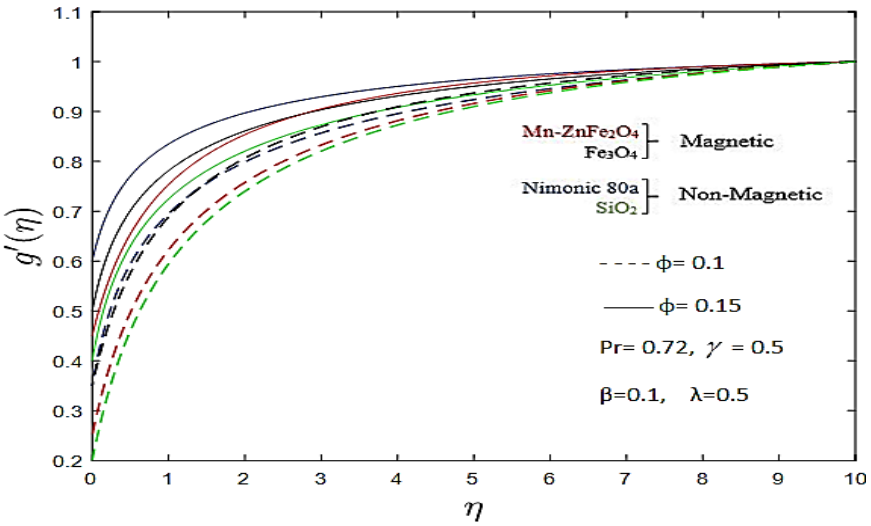

Figure 6b: Stream magnetic gradient function, $g'(\eta)$ for various ϕ and various nano-ferrofluids, with $\gamma = 0.5, 1, \beta = 0.1, \lambda = 0.5, \phi = 0.1, 0.15, \Pr = 0.72$

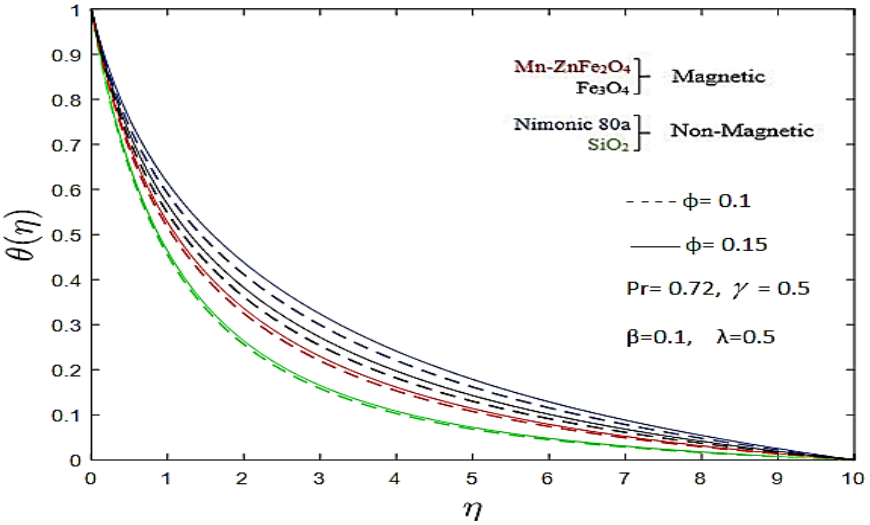

Figure 6c: Temperature distributions, $\theta(\eta)$ for various ϕ and various nano-ferrofluids, with $\gamma = 0.5, \beta = 0.1, \lambda = 0.5, \phi = 0.1, 0.15, \Pr = 0.72$

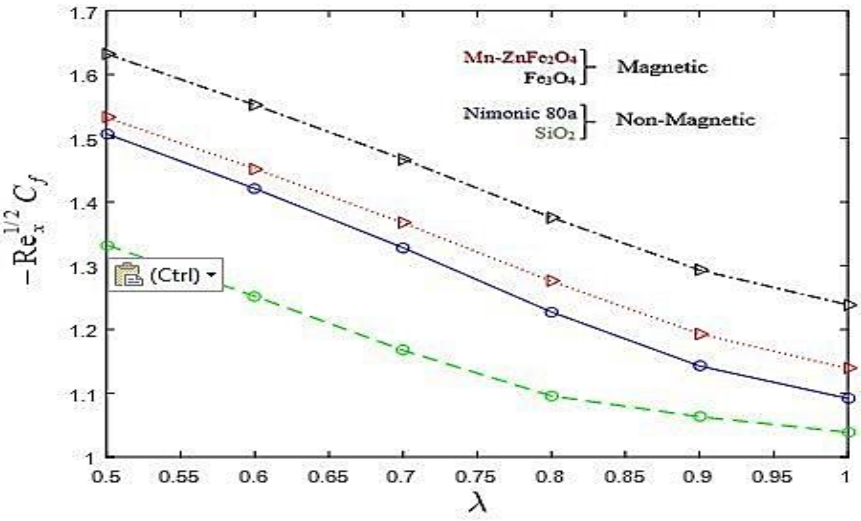

Figure 7a: Surface shear stress distribution, $f''(0)$ versus λ for different nano-ferrofluids, with γ=0.5, β=0.1, ϕ=0.1, Pr=0.72 .

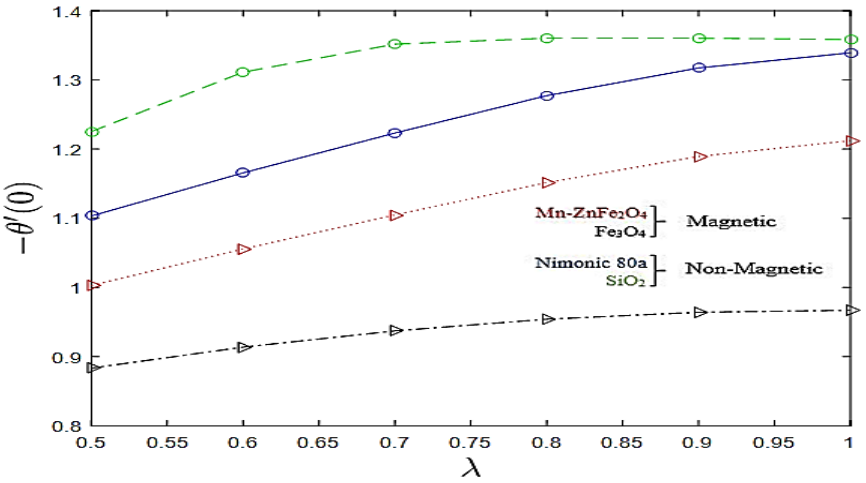

Figure 7b: Temperature gradient profiles, $\theta'(0)$ versus λ, for different nano-ferrofluids, with $\gamma = 0.5$, $\beta = 0.1$, $\phi = 0.1$, Pr = 0.72 .

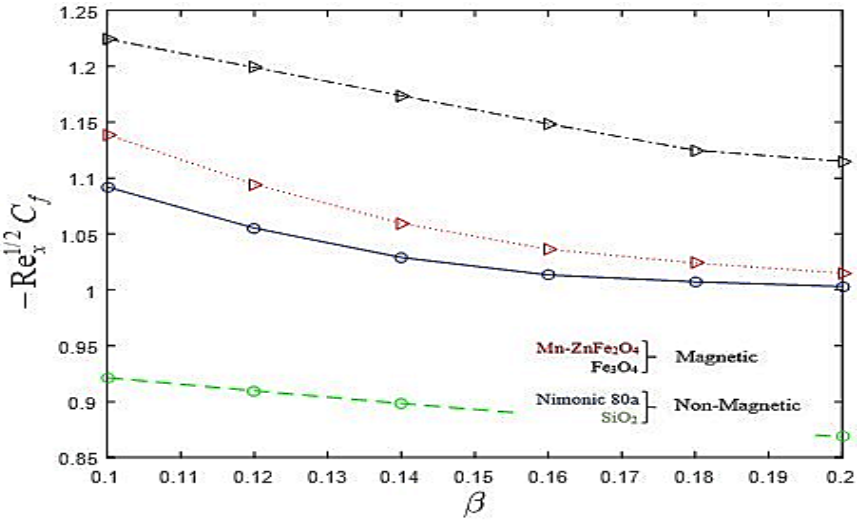

Figure 8a: Wall shear stress distribution, $f''(0)$ against β, for different nano-ferrofluids, with $\gamma = 0.5, 1$, $\lambda = 0.5$, $\phi = 0.1$, Pr = 0.72 .

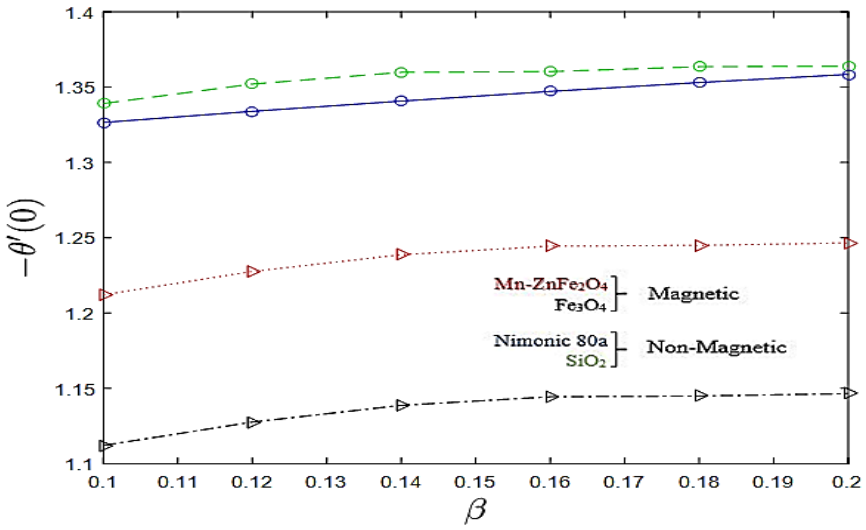

Figure 8b: Temperature gradient profiles, $\theta'(0)$ versus β, for different nano-ferrofluids, with $\gamma = 0.5, \lambda = 0.5, \phi = 0.1, \text{Pr} = 0.72$

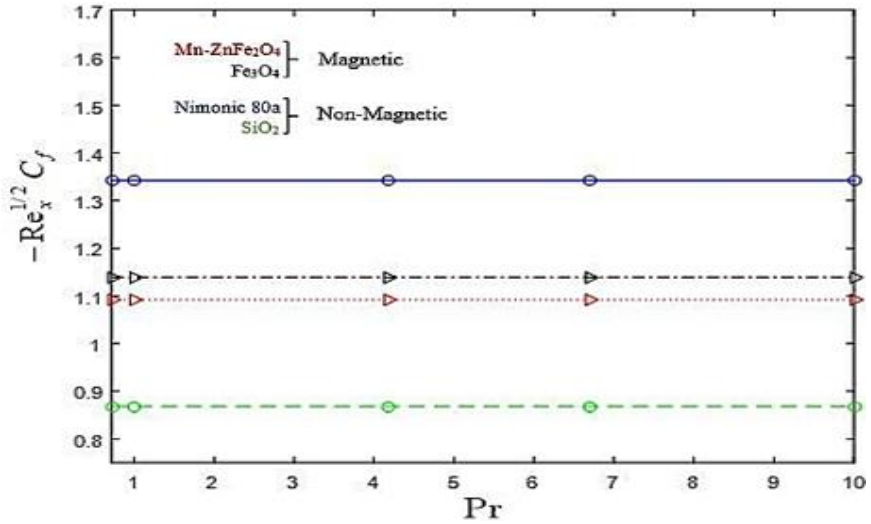

Figure 9a: Wall shear stress distribution, $f''(0)$ against Pr, for different nano-ferrofluids, with $\gamma = 0.5, \beta = 0.1, \phi = 0.1, \lambda = 0.5$.

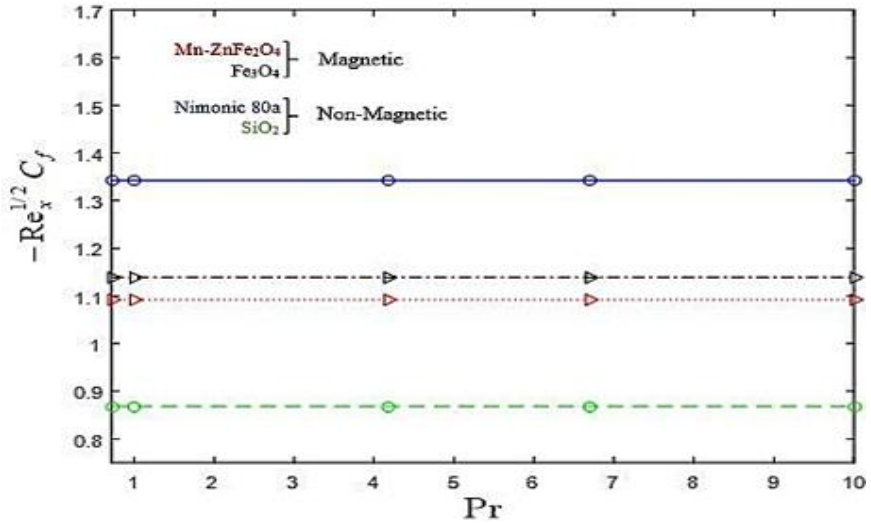

Figure 9b: Temperature gradient profiles, $\theta'(0)$ versus Pr for different nano-ferrofluids, with $\gamma = 0.5, \beta = 0.1, \phi = 0.1, \lambda = 0.5$

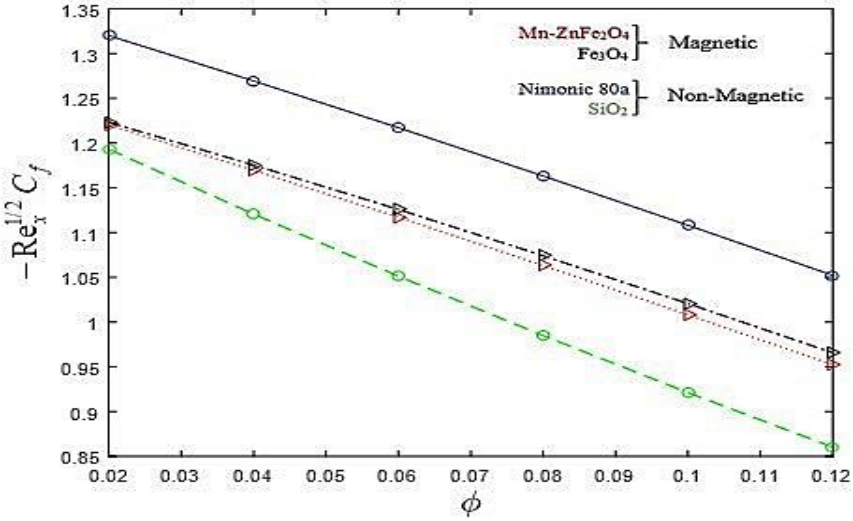

Figure 10a: Wall shear stress distribution, $f''(0)$ against ϕ, for different nano-ferrofluids, with $\gamma = 0.5, \beta = 0.1, \lambda = 0.5, \mathrm{Pr} = 0.72$.

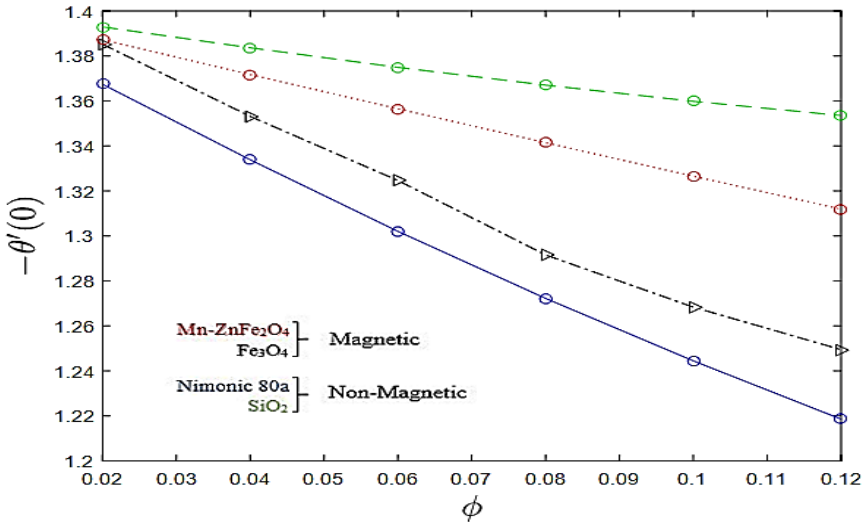

Figure 10b: Temperature gradient profiles, $\theta'(0)$ versus ϕ, for different nano-ferrofluids, with $\gamma = 0.5, \beta = 0.1, \lambda = 0.5, \mathrm{Pr} = 0.72$

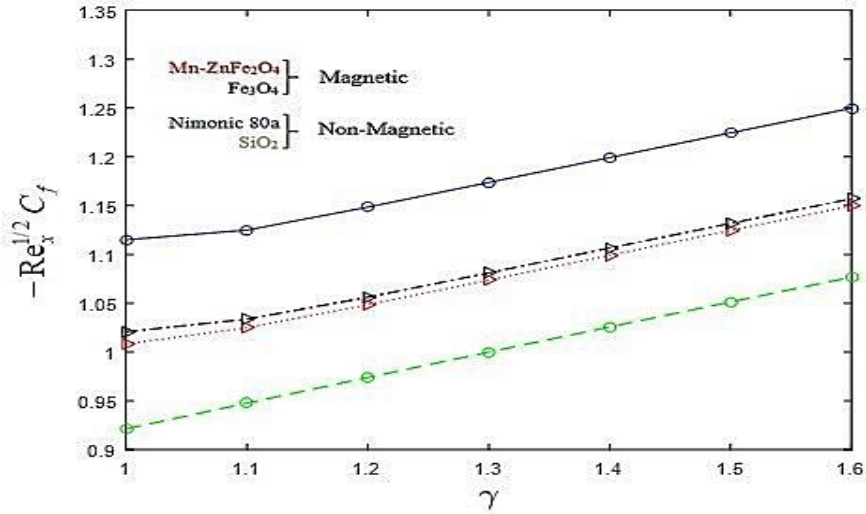

Figure 11a: Wall shear stress distribution, $f''(0)$ against γ, for different nano-ferrofluids, with $\lambda = 0.5, 1, \beta = 0.1, \phi = 0.1, \mathrm{Pr} = 0.72$

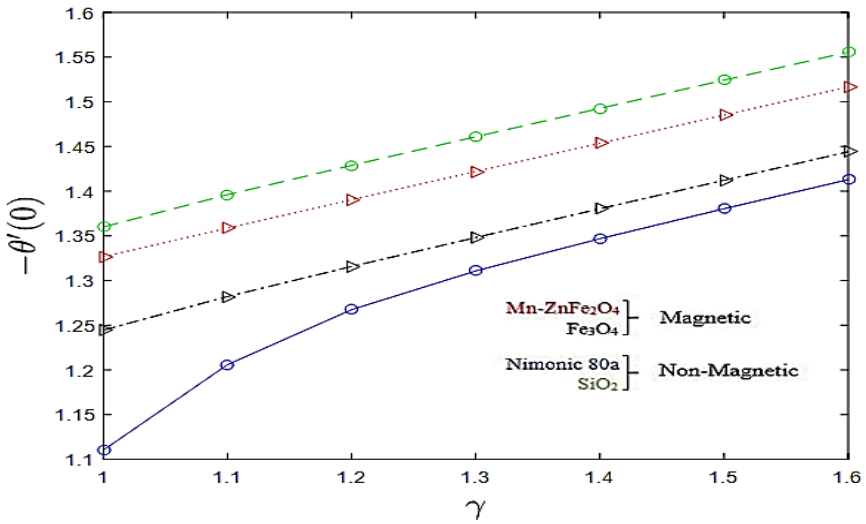

Figure 11b: Temperature gradient profiles, $\theta'(0)$ versus γ for different nano-ferrofluids, with $\lambda = 0.5, \beta = 0.1, \phi = 0.1, \mathrm{Pr} = 0.72$

Fig. 2a-c shows the evolution in $f'(\eta)$, $g'(\eta)$ and $\theta(\eta)$ profiles for different nano-ferrofluids (magnetic and non-magnetic) suspensions for variation in the inverse of Prandtl magnetic number, λ. Fig. 2a indications that the flow rate $f'(\eta)$ is highly reduced along the boundary layer with expanding numerical figures of λ. The non-magnetic nanoparticle SiO_2 shows high magnitude of velocity field (thinnest momentum boundary layer) while magnetic nanoparticle Fe_3O_4 displays lowest flow rate magnitude (thickest momentum boundary layer). Meanwhile, the remaining nanoparticles creates flow velocity at the two extremes with Mn-$ZnFe_2O_4$ lower than the Nimonic 80a for high computational figure of λ. Figure 2b exhibitions the impact of λ on the stream magnetic gradient function distributions $g'(\eta)$. As seen, increasing values of λ creates a support for the stream magnetic gradient function. In the observed situations, the flow distribution tends to a unity asymptotic in the far flow field. Magnetic Prandtl number [42, 56-58] expresses the rate of viscous distribution ratio to the rate of magnetic dispersion rate (i.e. the Reynolds magnetic number ratio to the regular Reynolds number). The term λ denotes the reciprocal ratio i.e. the rate of viscous diffusion dividing the rate of magnetic diffusion. Therefore, for $\lambda < 1$, the rate of viscous diffusion surpasses the rate of magnetic diffusion and otherwise for $\lambda > 1$. Whenever the magnetic diffusion controls intensifies, the impact of inducted magnetic shows high degrees of $g'(\eta)$ is attained for $\lambda = 2$ (boundary denser layer of magnetic field) and a repressed magnitudes of magnetic induction equivalent to $\lambda = 0.5$ (boundary thinner layer magnetic field) in fig. 2b. However, the converse effect is generated in the velocity field (fig. 2a) although no back flow is ever produced around the flow boundary film. Minimum values of $g'(\eta)$ are gotten for nanoparticles SiO_2, follow by Nimonic 80a Mn-$ZnFe_2O_4$ then Fe_3O_4. Obviously ferromagnetic properties are valuable to the induced magnetic field. Figure 2c illustrations that for high numerical

figures of λ, a separate temperature elevation is seen (and thermal boundary layer thickness). Higher relative diffused magnetic to viscous diffusivity is then supportive to the heat distribution process. Also, magneto-nanoparticles display considerably larger thermal conductivity augmentation when related to non-magneto nanoparticles, for instance, lowest amount of heats are generated by non-metallic SiO_2 follow by Nimonic 80a then Mn-$ZnFe_2O_4$, and finally by Fe_3O_4.

Fig 3a-c depict the evolution in velocity, magnetic induction and temperature distribution for different nanofluids (magnetic and non-magnetic) with Prandtl number (Pr). No tangible mitigation are computed either in velocity or in temperature (Figs. 3a, b) as Prandtl number changes. This invariance is largely associated with the forced convection flow nature and also the absence of magnetic field impacts on the Prandtl number (i.e. the expresses of the ratio of the viscous to the heat diffusion rates of the flow). Temperature (Fig. 3c) is clearly reduced with increasing Prandtl number (corresponding to a decrease in k_{nf}). This behavior is exhibited by both magnetic and non-magnetic nanoparticles. The temperature boundary layer viscosity is depleted with higher Prandtl number. The lowest heat transfer enhancement is associated with SiO_2, Fe_3O_4, Mn-ZnFe2O4 and Nimonic 80a in the respective order. Therefore, both the highest and lowest heat transfer enhancement is achieved by non-magnetic nanoparticles and the magnetic nanoparticle performance (Fe_3O_4, Mn-$ZnFe_2O_4$) falls between the Nimonic 80a and SiO_2 cases.

Figs. 4a-c visualize the influence of the body force magnetic term, β, on the $f'(\eta)$, $g'(\eta)$ and $\theta(\eta)$ function distribution for different nanofluids (magnetic and non-magnetic). Velocity profile (Fig. 4a) clearly decreases as β increases i.e. the flow momentum field declined in the device and the flow velocity boundary layer viscosity is increased and this is associated with the retarding nature of the body Lorentz force impact on the flow momentum Eqn. (14). Non-magneto nanoparticle, SiO_2 produces the maximum flow rate (strong flow acceleration) while magneto-nanoparticle Fe_3O_4 achieves the least flow rate (thickest momentum boundary layer thickness). Figure 4b indicates that increasing magnetic body force parameter, β results in an enhancement in the stream magnetic gradient function (magnetic induction). In the observed cases, minimum values are associated with the cylinder surface and these grow to a maximum in the free stream. Maximum magnetic induction is generated for Fe_3O_4 then by Mn-$ZnFe_2O_4$, follow by Nimonic 80a, and to the least by SiO_2. Fig. 4c shows that the magnetic nanoparticles achieve the best heat transfer enhancement i.e. least heats are obtained for SiO_2, then by Nimonic 80a follow by Mn-$ZnFe_2O_4$, and finally Fe_3O_4 in that order.

Fig. 5a-c shows the evolution in $f'(\eta)$, $g'(\eta)$ and $\theta(\eta)$ profiles with cylinder curvature parameter, $\gamma = \left(\sqrt{l\upsilon_f / U_0 a^2}\right)$. This parameter features in eqns. (14-(16). As cylinder radius increases clearly the curvature parameter is reduced (inverse relation). Conversely for smaller cylinder radius (decreasing cylinder surface area) there is a greater curvature effect which encourages momentum diffusion in the boundary layer and velocity enhancement (thinner momentum boundary layers), as also noted by Magyari et al. [14], among others. The highest velocity is achieved by SiO_2 then by Mn-$ZnFe_2O_4$, follow by Fe_3O_4 and finally by Nimonic 80a in the respective order. Stream magnetic gradient function (Fig. 5b) is also boosted with greater curvature effect indicating that a smaller surface area of the stretching cylinder is assistive to magnetic diffusion. Figure 5c clearly indicates that a slight raise in the heat is generated with greater cylinder curvature term and this creates a thermal boundary thicker layer. The highest heat transfer enhancement is achieved with the Nimonic 80a then by Fe_3O_4, follow by Mn-$ZnFe_2O_4$ then lastly SiO_2. The boost in temperatures is however less prominent when compared with velocity and magnetic induction over the same increment in curvature parameter.

Figs. 6a-c show the response in $f'(\eta)$, $g'(\eta)$ and $\theta(\eta)$ fields with the perpendicular coordinate of the volume fraction solid change term, ϕ, and various nanoliquid suspensions (magnetic and non-magnetic). Species mass doping of 10% and 15% are examined for ($\phi = 0.1, 0.15$). In figure 6a, it is obvious that a small declination of the flow with higher variation of fractional volume occurs i.e. the thickness of the flow velocity boundary layer reduces. The nanomaterial non-magnetic SiO_2 attains the peak flow rate, next by Mn-$ZnFe_2O_4$, follow by Fe_3O_4 and lastly by Nimonic 80a. The stream magnetic gradient function (fig. 6b) shows a significant boost with increasing fractional solid volume term. The impact is very noticeable close to the cylinder wall, increasingly shrinking towards the far stream. In figure 6c, it is clear that high stream magnetic gradient function is realized by SiO_2 next to it by Mn-$ZnFe_2O_4$, follow next is Fe_3O_4 and finally Nimonic 80a in the order. Fig. 6c displays a relative feeble rise in the nanoliquid heat distribution; a good thermal improvement is achieved for the nanofluid Nimonic 80a, next by Fe_3O_4, follow next is Mn-$ZnFe_2O_4$ and then by SiO_2. The same trend of temperature reaction is noticed as reported by [33, 53], though in the deficiency of induced magnetic field.

Figures 7a-b illustrate the coefficient of wall dragging friction and temperature gradient (Nusselt number) distributions for various rising values of inverse Prandtl magnetic number, λ. Clearly, the skin friction is reduced strongly with greater λ values indicating a significant deceleration of the flow boundary layer with depletion in the boundary layer hydrodynamic viscosity. Maximum skin friction coefficient corresponds to ferromagnetic nanoparticles i.e. Fe_3O_4 next to it is Mn-$ZnFe_2O_4$, then follow by Nimonic 80a and finally by SiO_2. However, there

is a substantial elevation in the rate of heat transport gradient to the cylinder wall (Nusselt number) with rising values of λ. Non-magnetic nanoparticles have a much larger Nusselt number than magnetic nanoparticles. SiO_2 has the highest Nusselt number followed by Nimonic 80a, Mn-$ZnFe_2O_4$ and Fe_3O_4 respectively.

Figs. 8a-b represent the reaction coefficient of wall friction and Nusselt number fields to changing in the magnetic term, β. As β increases (stronger applied magnetic field, H_o) the shear stress coefficient decreases indicating marked flow retardation. Again, the maximum skin friction coefficient is associated with Fe_3O_4 next to it is Mn-$ZnFe_2O_4$, follow next is Nimonic 80a and last to it is SiO_2 respectively. Increasing β values also elevate the Nusselt number at the cylinder surface. Non-magnetic nanoparticles produce higher Nusselt numbers (at any value of magnetic parameter) than magnetic nanoparticles. SiO_2 has the highest Nusselt number followed by Nimonic 80a, Mn-$ZnFe_2O_4$ and Fe_3O_4 (ferromagnetic) respectively.

Figs. 9a, b visualizes the evolution in skin friction and Nusselt number with Prandtl number. By varied range of Pr (<1 up to 10) there is no tangible modification in skin friction for any nanoparticle (legend is given in fig. 9b). The value of Nusselt number however significantly increases as Pr increases indicating the intensification in heat transferred to the cylinder surface from the nanofluid with progressively lower k_{nf}. SiO_2 has the highest Nusselt number then followed by Nimonic 80a, Mn-$ZnFe_2O_4$ and Fe_3O_4 respectively.

Figs. 10a, b illustrate the impact of solid fractional volume parameter ϕ on wall skin dragging force (dimensionless surface shear stress function) and Nusselt number for the investigated nano-particles. The computational figures for ϕ is taken between the figures 0.02 to 0.1, Qasim et al. [44] which aligns to 2% to 10% doping nanoparticle. As the value ϕ is raised, the coefficient of the shear stress reduces i.e. high induced flow shrinking is noticed. The nanoparticle non-magnetic Nimonic 80a reaches the maximum shear stress, and nanoparticle non-magnetic SiO_2 generate the smallest shear stress. On the other hand, Nusselt number (wall temperature gradient) decreases with solid volume fraction, since temperatures are increased (see earlier figures) and this confirms the effectiveness of nanofluids as superior thermal working fluids [25]. With reduction in Nusselt number there is a corresponding transfer of heat into the nanofluid leading to thicker thermal boundary layers [38-41]. Non-magnetic nanoparticles have the largest Nusselt numbers compared with magnetic nanoparticles which produce the lowest Nusselt numbers at any volume fraction. SiO_2 has the highest Nusselt number then followed by Nimonic 80a, Mn-$ZnFe_2O_4$ and Fe_3O_4 respectively.

Figs. 11a, b demonstration the variant in cylinder wall skin friction (dimensionless surface shear stress function) and Nusselt number again for all 4 nano-particles investigated, with cylinder curvature parameter γ. The values

of γ are selected in the range, 1 to 1.6 which is reasonable for industrial coating applications [13]. As the values of γ upsurges, the coefficient of shear stress declines. The nanoparticle non-magnetic Nimonic 80a attains the greatest shear stress, and the nanoparticle non-magnetic SiO_2 has the smallest shear stress, irrespective of curvature parameter value. However, there is a steady ascent in Nusselt number (wall temperature gradient) with increasing curvature parameter (smaller cylinder radius and curved surface area). Non-magnetic nanoparticles have the largest Nusselt number and magnetic nanoparticles produce the minimal Nusselt numbers. SiO_2 has the highest Nusselt number followed by Nimonic 80a, Mn-$ZnFe_2O_4$ and Fe_3O_4 respectively. Evidently therefore selectivity of the nature of nanoparticles is crucial in controlling surface heat transfer rates for cylinder coatings and both metallic (ferromagnetic) and non-metallic nanomaterials appear to have useful properties in this regard.

5. CONCLUSIONS

In the current study, a detailed mathematical construction of a steady state, incompressible, boundary layer flow of a nano-ferrofluid heat transfer past an extending cylinder is presented by a stimulated nanomaterial coating applications. Four different nanoparticles (two non-magnetic and two ferromagnetic) have been considered (SiO_2, Nimonic 80a, Mn-$ZnFe_2O_4$ and Fe_3O_4). A Tiwari-Das type fractional volume formation has been utilized to simulate nanoscale effects. The effects of magnetic induction and cylinder curvature have been included. By adopting a suitable transformation invariant quantities for the flow rate, energy transfer and magnetic field, the conservation equations have been converted to an ordinary derivative equations. The equations with suitable far stream and cylinder wall boundary conditions solved through SRM. Validation of solutions with earlier particular cases of the model available in the literature has been performed. Convergence performance of the SRM algorithm has also been examined. A detailed analysis of the impact of $\beta, \lambda, \mathrm{Pr}, \phi$, on momentum, magnetic induction and thermal characteristics (including coefficient skin friction and heat transfer gradient) has been accompanied. The current computational outcomes have revealed that:

- With higher magnetic body force parameter and inverse of Prandtl magnetic number, the flow is decelerated and momentum boundary layer thickness enhanced where the flow is energized i.e. temperature and thermal boundary layer thickness are elevated. Flow acceleration is enhanced with SiO_2 non-magnetic nanoparticles and good heat conduction augmentation is achieved with magnetic Fe_3O_4 nanoparticles.
- Rising Prandtl number has a trivial impact on velocity and magnetic induction whereas it significantly reduces temperature (and decreases the heat boundary layer thickness).

- Velocity, magnetic field and heat profile are all substantially enhanced with a rise in the cylinder curvature term (smaller surface contact area and cylinder radius).
- Rising fractional volume of the solid nanoparticle slows the flow velocity for both non-magnetic and magnetic nanoparticles whereas it elevates the magnetic induction and temperature.
- Coefficient of skin friction diminishes by a rise in the magnetic parameter, fractional volume solid nanoparticle term and inverse of Prandtl magnetic number (ratio of magnetic diffusion to viscous diffusion).
- Nusselt number upsurges by greater magnetic parameter, curvature term, fractional volume solid nanoparticle term and inverse of Prandtl magnetic number.
- Skin friction rises with a rise in the cylinder curvature parameter.
- Nusselt number reduces with a rise in the Prandtl number.
- Nanoparticle non-magnetic SiO_2 achieves the greatest flow rate enhancement.
- Ferromagnetic nanoparticle has the smallest flow rate enhancement that produces the best temperature enhancement.

The SRM numerical approach is an efficient and versatile technique for computational analysis of multi-physical nanoscale coating flows. It is currently also being explored for non-Newtonian ferromagnetic nanofluids using viscoelastic, viscoelastic and microstructural rheological models, and the results of these analyses will be reported, in the nearest time.

REFERENCES

[1] Schlichting H (1960) *Boundary-Layer Theory*, McGraw-Hill, New York, USA.

[2] Sakiadis BC, Boundary-layer behavior on continuous solid surfaces: I. Boundary-layer equations for two-dimensional and axisymmetric flow. AIChE J 1961;7(1): 26-28

[3] Sakiadis B (1961) Boundary-layer behavior on continuous solid surfaces: II. The boundary layer on a continuous flat surface. AIChE J, 7(2): 221-225.

[4] Crane LJ (1970) Flow past a stretching plate. Zeitschrift für angewandte Mathematik und Physik (ZAMP), 21(4):645-647.

[5] Salawu SO, Fatunmbi EO (2020) Current density and criticality branch-chain for a reactive Poiseuille second-grade hydromagnetic flow with variable electrical conductivity. International Journal of Thermofluids, 3-4, 100030.

[6] Dutta BK, Roy P, Gupta AS (1985) Temperature field in flow over a stretching sheet with uniform heat flux. Int Commun Heat and Mass Transfer, 12(1):89-94.

[7] Char MI (1988) Heat transfer of a continuous, stretching surface with suction or blowing. J Math Anal Applic, 135(2):568-580.

[8] Okedoye AM, Salawu SO (2019) Effect of nonlinear radiative heat and mass transfer on MHD flow over a stretching surface with variable conductivity and viscosity. J. of the Serbian Soc. for Comp. Mech., 13(2), 87-104.

[9] Cortell R (2005) Flow and heat transfer of a fluid through a porous medium over a stretching surface with internal heat generation/absorption and suction/blowing. Fluid Dynam Res, 37(4):231-245.

[10] Ferdows M, Shamshuddin MD, Zaimi K (2020) Dissipative radiative micropolar fluid transport in a non-Darcy porous medium with cross-diffusion effects. CFD Lett., 12(7): 70-89.

[11] Shamshuddin MD, Khan SU, **Anwar Bég O**, Beg TA (2020) Hall current, viscous and Joule heating effects on steady radiative 2-D magneto power-law polymer dynamics from an exponentially stretching sheet with power law velocity: A numerical study. Therm Sci Eng Prog, 20(1): Article ID:100732. https://doi.org/10.1016/.tsep.2020.100732

[12] Shamshuddin MD, Mishra SR, **Anwar Bég O, Beg TA** (2020) Computation of radiative Marangoni (thermocapillary) magnetohydrodynamic convection in Cu-water based nanofluid flow from a disk in porous media: Smart coating simulations, Heat Transf Res. https://doi.org/10.1002/htj.21963.

[13] Schwartz LW, Weidner DE (1995) Modeling of coating flows on curved surfaces. J Eng Math 29(1):91–103.

[14] Magyari E, Keller B, Pop I (2002) A note on the free convection from curved surfaces. ZAMM, 82(2):142-144.

[15] Datta P, Anilkumar D, Roy S, Mahanti NC (2006) Effect of non-uniform slot injection (suction) on a forced flow over a slender cylinder. Int J Heat and Mass Transfer, 49(13): 2366-2371.

[16] Elbarbary EME, Elgazery NS (2005) Flow and heat transfer of a micropolar fluid in an axisymmetric stagnation flow on a cylinder with variable properties and suction (numerical study). Acta Mech, 176(3-4):213-229.

[17] Khayat RE, Derdouri A (1994) Inflation of hyperelastic cylindrical membranes as applied to blow moulding. Part I. Axisymmetric case. Int J Numer Meth Eng, 37(22): 3773-3791.

[18] Luo YM, Chevalier L, Françoise U (2012) Modelling the heat during the injection stretch blowing moulding: Infrared heating and blowing modelling. ASME 2012 11th Biennial Conference on Engineering Systems Design and Analysis, July, Nantes, France.

[19] Prasad VR, Gaffar SA, Reddy, EK, **Anwar Bég O** (2014) Flow and heat transfer of Jefferys non-Newtonian fluid from a horizontal circular cylinder. AIAA J Thermophys Heat Transfer, 28:764-770.

[20] Basir MFM, Uddin MJ, Ismail AIA, **Anwar Bég O** (2016) Nanofluid slip flow over a stretching cylinder with Schmidt and Péclet number effects. AIP Adv, 6:055316-1 - 055316-15.

[21] Wang CY (1988) Fluid flow due to a stretching cylinder. Phys Fluids, 31(3):466-468.

[22] Ishak A, Nazar R, Pop I (2008) Magnetohydrodynamic (MHD) flow and heat transfer due to a stretching cylinder. Energy Conver Manag, 49(11):3265-3269.

[23] Ishak A, Nazar R. Pop I (2008) Uniform suction/blowing effect on flow and heat transfer due to a stretching cylinder. Appl Math Mod, 32(10):2059-2066.

[24] Butt AS, Ali A, Mehmood A (2016) Numerical investigation of magnetic field effects on entropy generation in viscous flow over a stretching cylinder embedded in a porous medium. Energy, 99:237-249.

[25] Nima NI. Salawu SO, Ferdows M Shamshuddin MD, Alsenafi A, Nakayama A (2020) Melting effect on non-Newtonian fluid flow in gyrotactic microorganism saturated non-darcy porous media with variable fluid properties. Applied Nanoscience, 10, 3911-3924.

[26] Ogunseye HA, Salawu SO, Tijani YO, Riliwan M, Sibanda P (2019) Dynamical analysis of hydromagnetic Brownian and thermophoresis effects of squeezing Eyring-Powell nanofluid flow with variable thermal conductivity and chemical reaction. Multidiscipline Modeling in Materials and Struct., 15(6), 1100-1120.

[27] Sandeep N, Sugunamma V, Mohankrishna P (2017) Effects of radiation on an unsteady natural convective flow of a EG-Nimonic 80a nanofluid past an infinite vertical plate. Adv Phys Theor Applic, 23, 36-43.

[28] Pandey AK, Kumar M (2017) Boundary layer flow and heat transfer analysis on Cu-water nanofluid flow over a stretching cylinder with slip. Alex Eng J, 56(4):671-677.

[29] Pankhurst QA, Thanh NTK, Jones SK, Dobson J (2009) Progress in applications of magnetic nanoparticles in biomedicine. J Phys D: Appl Phys, 42(22): 224001. https://doi.org/10.1088/0022-3727/42/22/220301

[30] Kashem MMA, Perlich J, Schulz, Roth SV, Muiller-Buschbaum P (2008) Correlated roughness in polymer films containing maghemite nanoparticles. Macromolecules, 41:2186-2194.

[31] Kashem MMA, Perlich J, Diethert A, Wang WN, Memesa M, Gutmann JS, Majkova E, Capek I, Roth SV, Petry W, Muiller-Buschbaum P (2009) Array of magnetic nanoparticles via particle co-operated self-assembly in block copolymer thin film. Macromolecules, 42: 6202-6208.

[32] Chiang YC, Chieh JJ, Ho CC (2012) The magnetic-nanofluid heat pipe with superior thermal properties through magnetic enhancement. Nanoscale Res Let, 7(1): 322. https://doi.org/10.1186/1556-276X-7-322.

[33] Shamshuddin MD, Mishra SR, **Anwar Bég O,** Kadir A (2019) Adomain decomposition method simulation of Von Karman swirling bioconvection nanofluid flow, Sci. Tech. Mining Metall., 26(10):2797-2813.

[34] Abdelsalam SI, Bhatti MM, Zeeshan A, Riaz A, Anwar Beg O (2019) Metachronal propulsion of magnetized particle-fluid suspension in a ciliated channel with heat and mass transfer. Physica Scripta, 94:115301 https://doi.org/10.1088/1402-4896/ab207a

[35] Lund LA, Omar Z, Khan I (2019) Quadruple solutions of mixed convection flow of magnetohydrodynamic nanofluid over exponentially vertical shrinking and stretching surfaces: stability analysis. Comput Met Prog Biomed, 182: Article ID: 105044. https://doi.org/10.1016/j.cmpb.2019.105044.

[36] Lund LA, Omar Z, Reza J, Khan I, Sherif EM (2020) Effects of Stefan blowing and slip conditions on unsteady MHD Casson nanofluid flow over an unsteady shrinking sheet: Dual solutions. Symmetry, 12: Article ID: 487. https://doi.org/10.3390/sym12030487

[37] Lund LA, Omar Z, Khan I, Seikh AH, Sherif EM, Nisar KS (2020) stability analysis and multiple solution of Cu-Al_2O_3/H_20 nanofluid contains hybrid nanomaterials over a shrinking surface in the presence of viscous dissipation. J Mat Res Tech, 9(1):421-432.

[38] **Anwar Bég O**, Kuharat S, Ferdows M, Das M, Kadir A, Shamshuddin MD (2019) Modelling magnetic nanopolymer flow with magnetic induction and nanoparticle solid volume fraction effects: solar magnetic nano-polymer fabrication simulation. Proc IMechE-Part N: J Nanoeng Nanomat Nanosyst, 233(1): 27-45.

[39] Rarani EM, Etesami N, Nasr EM (2012) Influence of the uniform electric field on viscosity of magnetic nanofluid (Fe3O4-EG). J Appl Phys, 112(9):094903. https://doi.org/10.1063/1.4763469

[40] Kandasamy R, Loganathan P, Arasu PP (2011) Scaling group transformation for MHD boundary-layer flow of a nanofluid past a vertical stretching surface in the presence of suction/injection. Nuclear Eng Design, 241(6):2053-2059.

[41] Shukla N, Rana P, **Anwar Bég O**, Kadir A, Bani S (2018) Unsteady electromagnetic radiative nanofluid stagnation-point flow from a stretching sheet with chemically reactive nanoparticles, Stefan blowing effect and entropy generation. Proc IMechE-Part N: J Nanoeng Nanomat Nanosyst, 232(2-3):69-82.

[42] **Anwar Bég O**, Ferdows M, Shamima S, Islam MN (2014) Numerical simulation of Marangoni magnetohydrodynamic bio-nanofluid convection from a non-isothermal surface with magnetic induction effects: a bio-nanomaterial manufacturing transport model. J Mech Medi Biol, 14(3):1450039.1-1450039.32.

[43] Sandeep N, Sulochana C, Isaac LA (2016) Stagnation-point flow of a Jeffrey nanofluid over a stretching surface with induced magnetic field and chemical reaction. Int J Eng Res Africa, 20:93-111.

[44] Qasim M, Khan ZH, Khan WA, Shah IA (2014) MHD boundary layer slip flow and heat transfer of ferrofluid along a stretching cylinder with prescribed heat flux. PloS one, 9(1): e83930. https://doi.org/10.1371/journal.pone.0083930

[45] Cramer KC, Pai SI (1973) Applied Magnetofluid Dynamics for Engineers and Applied Physicists. MacGraw-Hill, New York, USA.

[46] Motsa SS (2014) A new spectral relaxation method for similarity variable nonlinear boundary layer flow systems. Chem Eng Commun, 201(2):241-256

[47] **Anwar Bég O**, Motsa SS, Kadir A, **Bég TA**, Islam MN (2016) Spectral quasilinear numerical simulation of micropolar convective wall plumes in high permeability porous media. J Eng Thermophys, 25(4):1–24.

[48] **Anwar Bég O**, Motsa SS, Islam MN, Lockwood M (2014) Pseudo-spectral and variational iteration simulation of exothermically reacting Rivlin-Ericksen viscoelastic flow and heat transfer in a rocket propulsion duct. Comput Therm Sci, 6(2):91-102.

[49] Motsa SS, Makukula ZG (2013) On spectral relaxation method approach for steady von Kármán flow of a Reiner-Rivlin fluid with Joule heating, viscous dissipation and suction /injection. Cent Euro J Phys, 11(3):363-374.

[50] Awad FG, Motsa SS, Khumalo M (2014) Heat and mass transfer in unsteady rotating fluid flow with binary chemical reaction and activation energy. PloS one. 9(9): e107622. https://doi.org/10.1371/journal.pone.0107622

[51] Haroun NA, Sibanda P, Mondal S, Mosta SS (2015) On unsteady MHD mixed convection in a nanofluid due to a stretching/shrinking surface with suction/injection using the spectral relaxation method. Boundary Value Problems, 2015(1), 24. https://doi.org/10.1186/s13661-015-0289-5

[52] Canuto C, Hussaini MY, Quarteroni A, Zang TA (1988) Spectral Methods in Fluid Dynamics. Springer-Verlag, Berlin.

[53] Noghrehabadi A, Ghalambaz M, Ghalambaz M (2011) A theoretical investigation of SiO_2-water nanofluid heat transfer enhancement over an isothermal stretching sheet. Int J Multidis Sci Eng, 2(9):18-21.

[54] Wang CY (1989) Free convection on a vertical stretching surface. ZAMM, 69(11):418-420.

[55] Khan WA, Pop I (2010) Boundary-layer flow of a nanofluid past a stretching sheet. Int J Heat Mass Transfer, 53(11):2477-2483.

[56] Ghosh SK, **Anwar Bég O**, Zueco J, Prasad VR (2010) Transient hydromagnetic flow in a rotating channel permeated by an inclined magnetic field with magnetic induction and Maxwell displacement current effects. ZAMP, 61:147-169.

[57] Akbar NS, Tripathi D, Khan ZH, **Anwar Beg O** (2017) Mathematical model for ciliary-induced transport in MHD flow of Cu-H_2O nanofluids with magnetic induction. Chin J Phys, 55:947-962.

[58] Uddin MJ, Kabir MN, **Anwar Bég O**, Alginahi Y (2018) Chebyshev collocation computation of magneto-bioconvection nanofluid flow over a wedge with multiple slips and magnetic induction. Proc IMechE-Part N: J Nanoeng Nanomat Nanosyst, 232(4):109-122.